Heterogeneity and Hysteresis in the Polymer Collapse of Single Core-shell Stimuli-responsive Plasmonic Nanohybrids

Charlotte Flatebo,[1,2] Chayan Dutta,[2] Behnaz Ostovar,[3] Stephan Link,*[2,3,4] Christy F. Landes*[2,3,4,5]

[1]Applied Physics Program, [2]Department of Chemistry, [3]Department of Electrical and Computer Engineering, [4]Smalley-Curl Institute, and [5]Chemical and Biomolecular Engineering Department, Rice University, Houston, Texas 77005, United States

*Corresponding authors: slink@rice.edu (S.L), cflandes@rice.edu (C.F.L.)

Abstract

Broad application of polymeric stimuli-responsive smart nanohybrids requires understanding the mechanisms governing active control. Ensemble techniques have identified inhomogeneous polymer collapse in microgels that potentially arise from heterogeneous interchain interactions and differences in core size. A single-particle examination would establish the influence of core size and internal polymer network heterogeneity on local interactions that contribute to the observed inhomogeneous polymer collapse dynamics of nanohybrids. Using single-particle dark-field spectroscopy, we investigated the complex polymer collapse profiles of core-shell plasmonic nanohybrids comprising of thermoresponsive poly(N-isopropylacrylamide) (pNIPAM) encapsulated gold nanorods (AuNRs). We report that the polymer collapse behavior was independent of the core size. For thinner polymer shells, we observed hysteresis in the collapse of AuNR@pNIPAMs, likely related to local pNIPAM aggregation due to interchain hydrogen bonding. For thicker polymer shells, we observed a broad polymer collapse distribution that we attributed to a two-step phase transition that arises from a polymer network density gradient. Our single-particle approach relates the internal heterogeneity of the polymer network of nanohybrids to the mechanisms underlying heterogeneous phase transitions that traditional, ensemble-averaged approaches are unable to discern.

Keywords: nanohybrids; thermoresponsive polymer; active control; plasmonics; heterogeneity; nanoparticles

Introduction

Polymer-based stimuli-responsive smart materials are advancing adaptive sensing,[1–4] drug delivery,[5–8] catalysis,[9–11] and separations.[12–14] The switchable nature of the materials improves the overall performance through externally controlled "on" and "off" states. To achieve precise control over active materials at the macro- and nanoscale, the polymer composition must be optimized.[15–17] Increasing the cross-linker density increases the rigidity, which decreases the magnitude of polymer conformational changes.[18–20] Combining several stimuli-responsive monomers introduces multiple toggles to control the "on" and "off" states.[10,21] The combination of highly modular stimuli-responsive soft-materials with already promising inorganic nanomaterials results in a growing repository of smart nanohybrids for a broad range of applications.

Nanoscale insight into the mechanisms governing the phase transitions of stimuli-responsive nanohybrids is necessary. Theoretical modeling, neutron spin echo, and small-angle neutron scattering showed that polymer cross-linker density is highly variable, resulting in non-uniform swelling and collapse of the polymer matrix.[20,22–26] Transient absorption, UV-vis spectroscopy, and dynamic light scattering (DLS) demonstrated reversible collapse[16,27–30] and hysteresis[31–33] of stimuli-responsive polymers. For core-shell nanohybrids, although DLS reported single-step phase transitions, static light scattering and micro-differential scanning calorimetry revealed two-step polymer phase transitions that were attributed to surface curvature-induced polymer chain crowding.[17,34–36] These ensemble-averaged observations of stimuli-responsive nanohybrids preclude inferences into underlying differences between individual nanohybrids that arise from both the core size heterogeneity and the internal heterogeneity of the polymer network. Thus, it is possible that underlying heterogeneity in the core size and polymer network structure, which arises from variable monomeric units between cross-linking points, are nontrivial contributors to these inhomogeneous phase transitions of nanohybrids.[37] Because many potential applications of these smart materials rely on their nanoscale structure-function relationships, single-particle examinations of these relationships are necessary.

Single-particle techniques probe the dynamic stimuli-induced response of individual plasmonic nanohybrids. Cryo-transmission electron microscopy (TEM) and atomic force microscopy (AFM) can obtain the steady-state morphology,[15,38–40] whereas wet-AFM and liquid-cell TEM can probe the dynamic response of single stimuli-responsive nanohybrids.[41–43] To complement these morphological techniques, optical methods can observe the internal dynamics of single nanostructures.[44–48] Single-molecule fluorescence microscopy techniques have successfully interrogated three-dimensional morphological changes of polymer microgels.[47,48] However, the incorporation of plasmonic cores into the polymer matrix poses a problem for fluorescence-based methods due to efficient quenching.[49] To circumvent this complication, we use hyperspectral dark-field imaging to monitor the scattering spectra of plasmonic nanohybrids while undergoing temperature-induced collapse and expansion of the polymer shell as the changes of the single-particle plasmon resonance can be directly related to changes in the surrounding environment, especially near the interface between the nanoparticle core and the polymer shell.

In this work, we exploited the sensitivity of the plasmonic cores to interfacial changes to garner insight into the influence of underlying heterogeneity on stimuli-induced polymer phase transitions of core-shell nanohybrids. We synthesized thermoresponsive poly(N-isopropylacrylamide) (pNIPAM) encapsulating gold nanorods (AuNRs), shown in Figure 1A, and termed AuNR@pNIPAMs.[50] As depicted in Figure 1B, the pNIPAM shell experiences a reversible volume phase transition (VPT) near 32 °C, the lower critical solution temperature (LCST) of linear pNIPAM.[16,31,51] The VPT temperature (VPTT) is a function of both the LCST of linear chain pNIPAM and the cross-linker density and, as such, the VPTT typically ranges from 32-35 °C.[26,52] Above the VPTT, pNIPAM collapses and the refractive index (n) increases.[18] The plasmonic properties of the AuNR cores make them ideal sensors for changes in n because the longitudinal surface plasmon resonance energy peak (E_{res}) shifts in response to changes in the local n.[53–55] The observed resonance energy changes (ΔE_{res}) of AuNR@pNIPAMs were attributed to conformational changes of the polymer that led to local n changes. In addition, E_{res} is an indicator of AuNR size and shape,[56] which allowed us to investigate the influence of AuNR core size heterogeneity on polymer collapse. Using a calibrated heating laser to alternate the temperature between 25 °C (T_c) and 42 °C (T_h), we observed hysteresis and behavior consistent with two-step phase transitions of pNIPAM for single AuNR@pNIPAMs with minimal influence of AuNR core size.

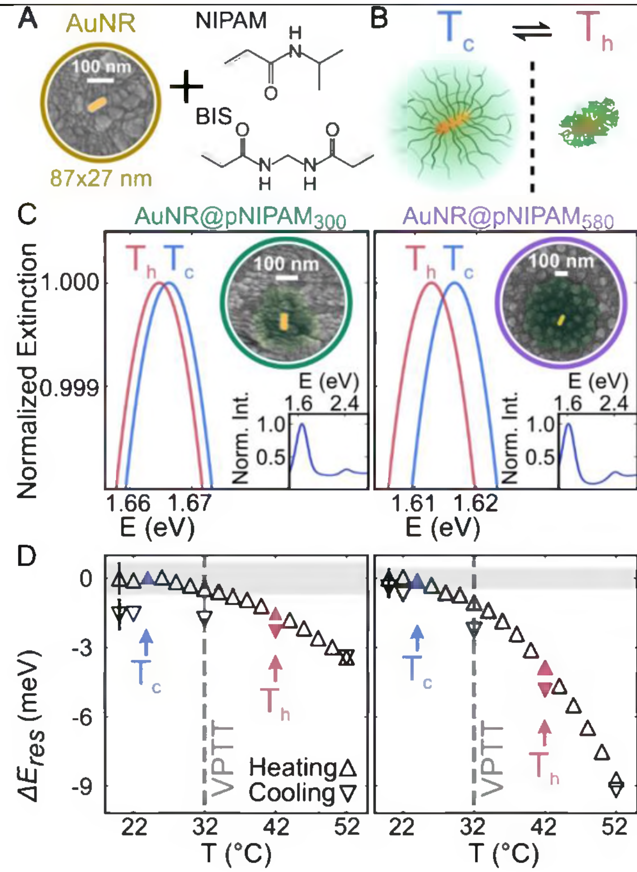

Figure 1. Synthesis and characterization of thermoresponsive AuNR@pNIPAMs. (A) Synthesis of nanohybrids for the free-radical seeded precipitation polymerization of pNIPAM from NIPAM monomers and BIS crosslinkers with AuNRs as the seeds. (B) Cartoon of AuNR@pNIPAMs in the expanded and collapsed forms at T_c and T_h, respectively. (C) Gaussian fits of the longitudinal surface plasmon resonance measured by temperature-controlled UV-vis spectroscopy of AuNR@pNIPAM$_{300}$ nanohybrids (left) and AuNR@pNIPAM$_{580}$ nanohybrids (right) at T_c and T_h. The top insets are false color SEM micrographs of the AuNR core (gold) and pNIPAM shell (green). Please note the scaling for each SEM micrograph. The bottom insets are the initial UV-vis spectra at 20 °C. (D) ΔE_{res} from the initial measurement at 20 °C as the sample was heated (Δ) and cooled (∇) for AuNR@pNIPAM$_{300}$ nanohybrids (left) and AuNR@pNIPAM$_{580}$ nanohybrids (right). The filled markers are the measurements at T_c and T_h. The horizontal gray bar represents the fitting error. The vertical line is the literature reported VPTT of pNIPAM.[51]

Methods

Core-shell AuNR@pNIPAM Synthesis

AuNRs were synthesized using the previously published sodium oleate method from the Murray group and were characterized with TEM and UV-vis spectroscopy (Figure S1).[57] To synthesize the nanohybrids, we followed the procedures developed by Contreras-Cáceres et al. for free-radical seeded precipitation polymerization of N-isopropylacrylamide (NIPAM, Sigma Aldrich, ≥99%) cross-linked with N,N'-methylenebisacrylamide (BIS, Sigma Aldrich, 99%) from the surface of AuNRs.[58] To do this, the capping ligands were replaced by vinylacetic acid (Alfa Aesar, 96%). The AuNRs were centrifuged at 7000 rpm for 30 minutes and then redispersed in 100 mL of water. The AuNRs were heated to 70°C and stirred at 700 rpm. Once 70°C was reached, 600 µL of vinylacetic acid was added to the solution and left to react for 1 hour.[58,59] The AuNRs were centrifuged at 7000 rpm for 30 minutes, the supernatant was removed and the AuNRs were redispersed in 50 mL of water. The 84 × 26 nm AuNRs were added to 56.6 mg NIPAM and 7.7 mg BIS (10 mM NIPAM, 10 mol% BIS) and are termed AuNR@pNIPAM$_{300}$ nanohybrids. The 89 × 28 nm AuNRs were added to 96.8 mg NIPAM and 13.1 mg BIS (17 mM NIPAM, 10 mol% BIS) and are termed AuNR@pNIPAM$_{580}$ nanohybrids. The solutions were equilibrated for 15 minutes at 70 °C and stirred at 400 rpm under bubbled ultrapure nitrogen in a water-cooled reflux system. Once equilibrated, 100 µL of 0.1 M 2,2'-Azobis(2-methylpropionamidine) dihydrochloride (Matrix Scientific, 95+%) was injected into the solution and the reaction proceeded for 1 hour. The nanohybrids were then centrifuged for 45 minutes at 9000 rpm and then redispersed in water. The AuNR@pNIPAMs were stored at room temperature.

Ensemble Characterization

The nanohybrids were characterized with DLS and UV-vis spectroscopy. DLS (Malvern Zen 3600 Zetasizer) measurements of AuNR@pNIPAM$_{300}$ nanohybrids and AuNR@pNIPAM$_{580}$ nanohybrids at 20 °C and 50 °C can be found in Table S1. At all temperatures, AuNRs registered as 96 ± 6 nm for the 84 × 26 nm AuNRs and 120 ± 20 nm for the 89 × 28 nm AuNRs and can also be found in Table S1. For UV-vis temperature-controlled measurements, a Jasco J-1500 CD spectrometer with a Peltier thermostatted single position cell holder was used. A spectrum, with a spectral resolution of 0.1 nm, was taken every 2 °C, from 20 to 52 °C, and then at 52, 42, 22, and 20 °C (Figure 1C, 1D, and S2A). The UV-vis spectra were fit to a Gaussian to account for the inhomogeneous broadening that results from the heterogeneity of the colloidal AuNR cores.[60]

Water Cell Preparation

The nanoparticles were spincast on the surface of oxygen plasma-cleaned transparent indium tin oxide (ITO) coated substrates (Evaporated Coatings Incorporated, 55 ohm/sq, 22 × 22 mm glass coverslips) for 1 minute at 4000 rpm with an acceleration of 2000 rpm. The hydrophilic surface of the substrate minimizes the interaction between pNIPAM and the surface, which is conducive to pNIPAM microgels maintaining their spherical shape and stimuli-responsive dynamics.[47] All nanoparticle solutions were diluted to achieve an average particle density of ~3 particles per 100 μm^2. Using a low particle density, we avoided interparticle plasmon coupling that could impact observed ΔE_{res}.[61] To create a water cell, two adhesive spacers (Grace Bio-Laboratories, 0.12 mm thick) and a modified silicon spacer (Grace Bio-Laboratories, 0.5 mm thick) were placed on the ITO substrates. A neutral solution of 10 mM HEPES (Sigma Aldrich) in water was used to fill the cell. A glass coverslip was placed on top of the cell and the cell was pressure sealed between two aluminum plates.

Hyperspectral Dark-Field Imaging and Heating Apparatus

To investigate the optical response of the AuNR@pNIPAMs, we used a homebuilt hyperspectral microscope, described in detail in a previous publication.[46] Briefly, an inverted microscope (Zeiss AxioObserver m1) fitted with a dark-field condenser (NA = 1.4) illuminated the sample with white light from a 100 W halogen lamp and a collection objective (Zeiss PlanAchromat 63x, variable NA set to 0.7) collected the scattered light from the nanoparticles. With the microscope internal 1.6x magnification, the total magnification was 100.8x. The scattered light was directed through a slit with a width of 20 µm onto a grating (150 gr/mm, 800 nm blaze wavelength) in a spectrograph (Princeton Instruments, Acton SP2150i). The dispersed light was collected with a charge-coupled device camera (Princeton Instruments, PIXIS 400). The camera and spectrograph were mounted on an electronically driven translation stage (Newport Linear Actuator, LTA-HL) that scanned across the field of view to create a hyperspectral datacube using custom LabVIEW software (National Instruments). A 1064 nm heating laser (Cobalt Rumba 3000, continuous wave) was aligned in wide-field epifluorescence configuration. To direct the laser to the sample, a dichroic mirror was used (Semrock NFD01-1064-25-D). A 1000 nm shortpass filter (ThorLabs DMSP1000) was placed in the detection path to remove residual heating laser excitation.

To control the temperature in the thin water cell, we created a calibration curve that relates the output power of the heating laser to the temperature in the field of view. This calibration was done by building a cell containing a thermocouple (Omega, 5SC-TT-K-40-36) and monitoring the temperature of the water as the laser power was increased. For continuous wave wide-field epifluorescence illumination, the temperature should achieve thermal equilibrium within the focal volume of the laser spanning the thickness of the water cell.[62,63] As the ITO substrate is a reasonable heat conductor, it is possible that the substrate under laser illumination is at a higher temperature than what the thermocouple reports. However, ITO absorption at 1064 nm is negligible and does not increase the local temperature the particles experience.[64,65] Without laser illumination, the temperature of the water reached a maximum temperature of 25°C, below the published VPTT of pNIPAM microgels with similar crosslinking densities.[16] Because the objective absorbs ~65% of the photons at 1064 nm and the damage threshold is unknown, we selected the laser power that achieved a temperature 10°C above the published VPTT, which we hypothesized would be sufficient to achieve complete polymer collapse of the nanohybrids while preventing irreversible thermal damage to the objective.

Data Acquisition and Analysis of Single Particles

Three hyperspectral scattering images of ~1500 μm^2 were acquired prior to heating at T_c. Turning the heating laser on and off, the sample was cycled between T_h and T_c four times and a hyperspectral image was acquired at each temperature. After the final T_c measurement, two additional hyperspectral images were taken at T_c. Although polymer collapse and expansion are considered to be nearly instantaneous,[24,28,30] we equilibrated the sample for five minutes in the dark between acquisitions to allow the temperature to stabilize and the complete expansion/collapse of the polymer. The pixel integration time was 3 s for an overall image acquisition time of ~7.5 minutes.

All data was analyzed with Python 2.7. After hyperspectral image processing, all particle spectra were fit to a single Lorentzian prior to normalization. Normalized spectra are shown for better comparison of ΔE_{res} and the spectra prior to normalization of the representative single-particles for each sample can be found in Figure S3. Acquiring single-particle spectra avoids the inhomogeneous linewidth broadening observed in the ensemble spectra and, as such, a Lorentzian profile provides a more accurate physical description of the spectra.[66,67] To limit the analysis of aggregates, particles with an intensity greater than twice the median intensity were removed. Spectral fits with intensities in the lowest 5% were discarded to remove particles with low signal to noise ratios that would result in large errors in the fit parameters. To determine the limit of detection for ΔE_{res}, the standard deviations of E_{res} of the first three and last three measurements of the remaining particles were averaged (±0.5 meV). The average of the first three measurements determined the initial E_{res} for each particle. Although changes in intensity are also observed (Figure S3), ΔE_{res} appears to be a more straightforward indicator of reversible polymer collapse. An in-house image processing Python script using scikit-image modules was used to determine the diameter of the polymer shell from scanning electron microscopy (SEM) micrographs.[68]

Finite Difference Time Domain (FDTD) Simulations

The commercial software package Lumerical FDTD Solutions was used to simulate the scattering cross-sections of AuNRs in various experimental conditions. A hemisphere capped cylinder was chosen to model the geometry of the AuNRs. All simulations were performed using an AuNR with dimensions of 87 × 27 nm, the average size of the AuNRs studied in this work. The dielectric function for gold was extracted from the measured values by Johnson and Christy and Olmon et al.[69,70] A semi-infinite ITO substrate with n of 1.86 was used to model the substrate in single-particle measurements. The computational mesh size was set to 1 nm (unless otherwise stated), and the default convergence criteria were used. Perfectly matched layers were employed around the entire system.

For the simulations of AuNRs in water with different temperatures, the temperature-dependent n of water (Figure S2B) were calculated using the equation and fitting parameters from Thormählen et al. and used as the background.[71] The computational mesh size was set to 0.5 nm.

To capture the effect of polymer collapse on the AuNR scattering cross-section, we simulated the conditions replicating the phase transition extremes: expanded and collapsed. When expanded, the local AuNR environment is predominantly water, with limited contributions from pNIPAM.[18] When pNIPAM collapses, pNIPAM's contribution to the local n increases with the expulsion of water. Thus, we used a n of 1.37 to represent the expanded, water-rich pNIPAM shell and a n of 1.46 to represent the collapsed, water-poor pNIPAM shell to model the effect of polymer collapse on the AuNR scattering cross-sections.[18,72] To further mimic experimental conditions, the pNIPAM shell was set to 100 nm for the expanded condition and 5 nm for the collapsed condition. Figure S4A illustrates the simulation technique employed to estimate the AuNR sensing volume, i.e. the average volume from the AuNR surface where a change in n can no longer be detected.[73] It is important to note that the effect of the ITO substrate on ΔE_{res} becomes evident only when the polymer collapses within the sensing volume of the AuNR (~36 nm) and the n of ITO contributes to the total n experienced by the AuNR (Figure S4B).

Results & Discussion

AuNR@pNIPAMs with two different polymer shell thicknesses were synthesized as described in the Methods section.[57–59] The AuNR@pNIPAMs were characterized by SEM, shown in Figure 1C insets, and had average diameters of 300 ± 40 nm (AuNR@pNIPAM$_{300}$) and 580 ± 20 nm (AuNR@pNIPAM$_{580}$). Temperature-dependent DLS measurements (Table S1) at 20 °C revealed slightly different sizes, with AuNR@pNIPAM$_{300}$ nanohybrids and AuNR@pNIPAM$_{580}$ nanohybrids having average diameters of 333 ± 4 nm and 530 ± 10 nm, respectively. At 50 °C, above the VPTT, both AuNR@pNIPAMs collapsed to similar DLS-determined sizes of 130 ± 4 nm and 130 ± 1 nm, respectively. It is important to note that the DLS cumulant fit assumes isotropic scatterers and, in the case of the expanded nanohybrids, is likely a reasonable approximation of the size, especially when compared with the dimensions extracted from the SEM micrographs. However, in the case of the collapsed nanohybrids, the shell thickness is at least 82% smaller than the longest dimension of the core, resulting in anisotropic scatterers that require applying theoretical models to depolarized DLS to extract the precise dimensions.[74,75] Thus, our DLS measurements serve as an initial verification and qualitative approximation of the temperature-induced VPT rather than to determine the absolute sizes. The similar diameters measured at 50 °C for the two AuNR@pNIPAM samples may be the result of the much thinner, collapsed polymer shells and, therefore, the AuNR core size dominated the overall hydrodynamic dimensions. Note that the size distributions of the AuNRs used were almost the same (see Figure S1). AuNRs did not exhibit temperature-induced changes in hydrodynamic diameter (see Ensemble Characterization in the Methods section).

When heated, the ensemble E_{res} of AuNR@pNIPAMs decreased in energy. We performed temperature-controlled UV-vis spectroscopy to observe the ensemble ΔE_{res} of colloidally suspended AuNR@pNIPAMs. Figure 1C illustrates that increasing the temperature from T_c to T_h decreases E_{res} by 1.5 ± 0.7 meV for AuNR@pNIPAM$_{300}$ nanohybrids and by 3.6 ± 0.4 meV for AuNR@pNIPAM$_{580}$ nanohybrids. This decrease in E_{res} is attributed to an increase in n of the collapsed polymer, which has been observed and predicted previously for pNIPAM on Au nanospheres.[52,55] For fully collapsed shells for both types of nanohybrids, the water environment will also contribute to the average n experienced by the cores. The observed larger ΔE_{res} for the AuNR@pNIPAM$_{580}$ nanohybrids can be explained considering that increasing the molecular weight of the polymer network increases the effective collapsed polymer shell n experienced by the plasmon.[55,76] Additionally, ΔE_{res} does not plateau above the VPTT as observed previously for gold nanospheres, which may result from the higher sensitivity of AuNR cores to local n changes.[16,18,52,53] The steady decrease in ΔE_{res} above the VPTT may also arise from heterogeneity in the VPTT of individual nanohybrids resulting from inhomogeneous cross-linker distribution or polymer density gradients.[17,23] In contrast, the E_{res} of AuNRs increased by 4 ± 2 meV when heated as a result of the decrease in n of water with increasing temperature (Figure S2).[71]

Upon cooling, the ensemble ΔE_{res} of AuNR@pNIPAM$_{300}$ nanohybrids exhibited hysteresis, whereas the ΔE_{res} of AuNR@pNIPAM$_{580}$ nanohybrids did not. When cooled, the AuNR@pNIPAM$_{300}$ nanohybrids exhibited a 1.6 meV decrease in E_{res} between the initial and final 20 °C measurements, indicative of hysteresis (Figure 1D, left). Conversely, E_{res} of AuNR@pNIPAM$_{580}$ nanohybrids returned to the initial value upon cooling and did not exhibit

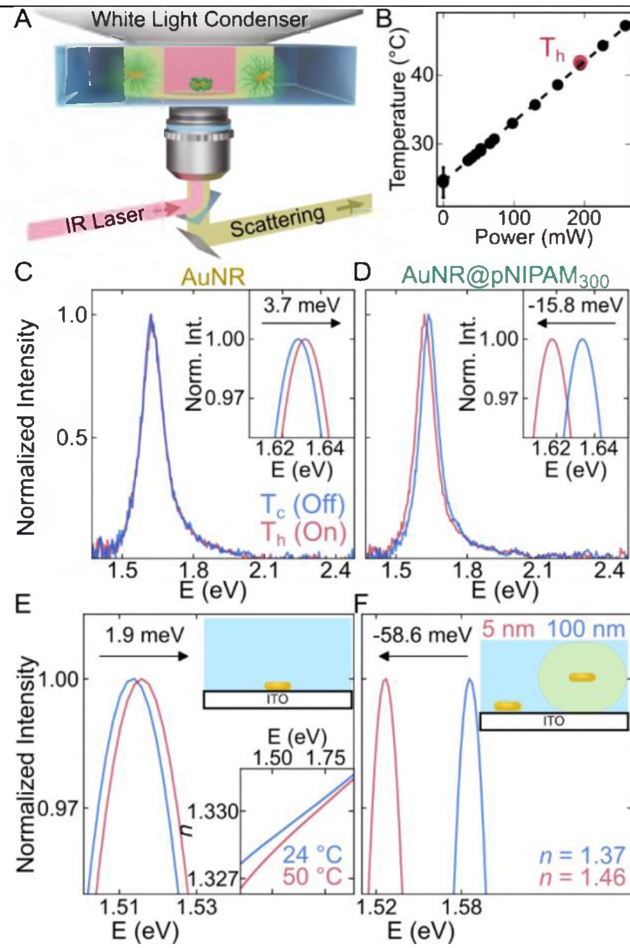

Figure 2. Single-particle measurements and the relationship between ΔE_{res} and changes in n. (A) Schematic of dark-field excitation and heating laser illumination of particles in a closed aqueous cell. (B) Calibration curve of the temperature as a function of laser power. The error bar is the same for all points. The red marker indicates the power used to achieve T_h. Representative spectra of an (C) AuNR and (D) AuNR@pNIPAM300at T_c (laser off) and T_h (laser on). Insets are the Lorentzian fits at T_c and T_h. (E) FDTD simulated scattering cross-sections of an 87 × 27 nm AuNR on an ITO substrate in water. Inset is the calculated n of water at 24 °C (blue) and 50 °C (red) employed in the simulations. (F) FDTD simulated scattering cross-sections of an 87 × 27 nm AuNR with a 100 nm thick shell with n of 1.37 (blue) and a 5 nm thick shell with n of 1.46 (red) in water on an ITO substrate.

hysteresis (Figure 1D, right). Hysteresis in pNIPAM phase transitions has previously been observed and may arise from dissimilar polymer network density or from interchain hydrogen bonds that form aggregates that persist even after cooling below the VPTT for the AuNR@pNIPAM300 nanohybrids.[17,31,32,77–80]

Single-particle hyperspectral dark-field spectroscopy showed that the direction of E_{res} shifts was consistent between single-particle and ensemble measurements. The nanoparticles were spincast onto a transparent substrate, sealed in a liquid cell, and imaged with a hyperspectral dark-field microscope as described in the Experimental Section.[46] A near-infrared laser was aligned into the microscope in a wide-field, epifluorescence configuration to heat the aqueous environment as depicted in Figure 2A. Figure 2B is the calibration curve that relates the laser power to the temperature of the sample in the field of view. We used a laser power of 194 mW to raise the temperature above the VPTT to T_h (Figure 2B, red marker). Figure 2C and 2D illustrate that, under laser illumination, E_{res} increased by 3.7 meV for a representative AuNR and decreased by 15.8 meV for a representative AuNR@pNIPAM$_{300}$, consistent with the direction of ensemble E_{res} shifts.

FDTD simulations of scattering cross-sections confirmed the trend of experimentally observed ΔE_{res}. FDTD calculated E_{res} of an 87 × 27 nm AuNR increased by 1.9 meV as the temperature of the water-only environment increased from 24 and 50 °C due to the temperature dependence of n of water (Figure 2E). The simulated results are consistent with the temperature-dependent ensemble UV-vis measurements of bare AuNRs (Figure S2). To model the pNIPAM environment surrounding the AuNR core, we simulated the two extremes of the pNIPAM phase transition. When the pNIPAM shell is expanded, the environment surrounding the AuNR core is predominantly water and pNIPAM has limited influence on n.[18] With pNIPAM collapse, the water is expelled and the contribution of pNIPAM to the local n increases. Therefore, we modeled the expanded pNIPAM shell as a water-rich environment with n of 1.37 and the collapsed pNIPAM shell as a water-poor, polymer-rich environment with n of 1.46.[72] To represent the collapsed state, a 5 nm pNIPAM shell thickness was used to represent the shell thickness at 50 °C (see Table S1 for temperature-dependent DLS swelling measurements). To represent the expanded state, the thickness was set to 100 nm, larger than the ~36 nm sensing volume of the AuNR (see discussion in the Supporting Information under Figure S4). Taking into account the temperature-dependent n of water and the ITO substrate, our simulations report a 58.6 meV decrease in E_{res} with polymer collapse, which agree with the experimentally observed decrease in E_{res}. The FDTD simulations correctly predict the direction of ΔE_{res}, but overestimate the magnitude.

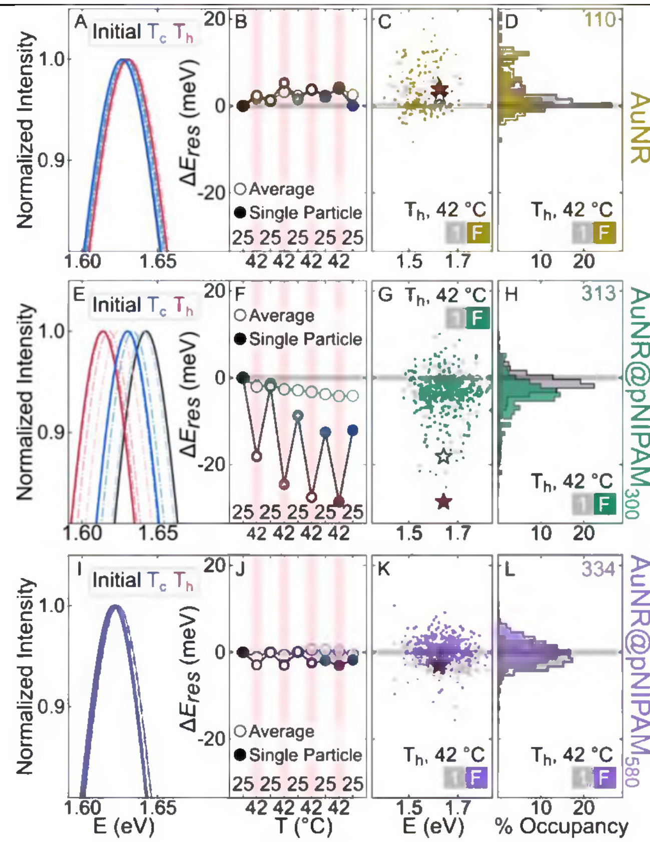

Figure 3. Reversibility and hysteresis in single particle spectra in response to temperature cycling. (A-D) AuNR, (E-H) AuNR@pNIPAM300, and (I-L) AuNR@pNIPAM580 . (A, E, I) Lorentzian fits of the longitudinal plasmon resonance of representative single particles. The solid lines indicate the initial (black), final T_c (25 °C, blue), and final T_h (42 °C, red) measurements. The dashed lines indicate the intermediate T_c and T_h measurements. (B, F, J) Corresponding ΔE_{res} (●) at successive T_c and T_h. The vertical red bars indicate T_h. The average ΔE_{res} of all single particles (○) is included for comparison. (C, G, K) Scatter plots of ΔE_{res} at the first and final T_h for all single particles measured. The stars are the representative particles from A, E, and I, respectively. (D, H, L) Histograms of ΔE_{res} for the first and final T_h with the number of particles measured listed in the upper right corner. The horizontal gray bar in all plots represents the limit of detection of the instrument (±0.5 meV).

Considering the good agreement between experimental results and theory for the bare AuNRs in Figure 2C and 2E, we attribute the overestimation of ΔE_{res} of simulated AuNR@pNIPAMs to the limitations of our model that arose from unknown parameters of the polymer shell. The FDTD simulations did not account for the polymer network density at the surface of the AuNRs or the polymer density gradients spanning the pNIPAM shell, as neither of these parameters are known at the single-particle level.[17,55] Additionally, the cross-linker density, which determines the polymer volume fraction of the collapsed shell, likely varies throughout the polymer shell, consequently varying n within the sensing volume of the core.[20,55,72] We note that the choice of gold dielectric data also did not explain the observed overestimation (Figure S5). In light of the simplifications imposed upon the FDTD model by the unknown parameters discussed above, it is not surprising that a quantitative agreement was not achieved for the magnitude of ΔE_{res}, consistent with Tagliazucchi et al.[55]

ΔE_{res} of single particles was reversible and followed the average trend of the population. Figure 3A and 3B show that E_{res} of a representative AuNR increased by an average of 3.8 meV at T_h. At T_h, E_{res} of representative AuNR@pNIPAM$_{300}$ and AuNR@pNIPAM$_{580}$ nanohybrids decreased an average of 24.7 meV and 2.9 meV, respectively (Figure 3E, 3F, 3I and 3J). At T_c, E_{res} shifted in the reverse direction. Additional spectra of single particles in Figure S6-S8 illustrate that the magnitude of ΔE_{res} varied between particles, but followed the average trend of the population.

The magnitude of ΔE_{res} was independent of core size within the AuNR sample size distributions. Figure 3C, 3G, and 3K indicate that, although ΔE_{res} varied between particles, the magnitude was independent of the initial E_{res} and, accordingly, the core size. The variation in ΔE_{res} magnitudes could arise from differing polymer network chain lengths that would change the n of the polymer shells, but this effect is unlikely because the measured AuNR@pNIPAM diameters only varied by 20 to 40 nm based on SEM measurements.[76] Alternatively, heterogeneous polymer network density could account for the variable ΔE_{res} observed.[24,55] Overall, we obtained core-independent trends that, at T_h, E_{res} increased for AuNRs, decreased for AuNR@pNIPAM$_{300}$ nanohybrids, and exhibited minimal changes for AuNR@pNIPAM$_{580}$ nanohybrids.

Single AuNR@pNIPAM$_{300}$ nanohybrids exhibited hysteresis of ΔE_{res} with additional temperature cycling between T_c and T_h. Figure 3E and 3F illustrate that E_{res} of the representative AuNR@pNIPAM$_{300}$ did not return to the initial E_{res} at T_c, and the magnitude of this difference increased with additional cycles. Figure 3G and 3H also indicate that the majority of AuNR@pNIPAM$_{300}$ nanohybrids experienced hysteresis, indicated by the growing shift of ΔE_{res} between the first and final T_h. With successive T_c, E_{res} decreased in energy as compared to the initial E_{res} for AuNR@pNIPAM$_{300}$ nanohybrids, but not AuNR@pNIPAM$_{580}$ nanohybrids (Figure S9). This observation agrees with our ensemble UV-vis measurements. Hysteresis in the VPT of pNIPAM results from pNIPAM aggregates formed by interchain hydrogen bonds that are not disrupted when cooled.[32,77–79] This likelihood of pNIPAM aggregate formation decreases with increasing polymer network chain length, which accounts for the limited hysteresis observed for AuNR@pNIPAM$_{580}$ nanohybrids.[78]

For AuNR@pNIPAM$_{580}$ nanohybrids, the broad distribution and unexpected minimal changes in ΔE_{res} indicate competing factors that govern the local n the core observes. Based on ensemble results (Figure 1), we expected at least twice the average ΔE_{res} for AuNR@pNIPAM$_{580}$ nanohybrids than AuNR@pNIPAM$_{300}$ nanohybrids, which was not observed in Figure 3I-3L (see Table S2). It is possible that T_h is lower than the VPTT for the AuNR@pNIPAM$_{580}$ nanohybrids. However, we observe large changes in the peak intensity at T_h that may arise from either a decrease in size of the polymer shell or an increase in the local n observed (Figure S10).[56] These large changes in intensity, in concert with the ensemble UV-vis ΔE_{res}, support that T_h is sufficient to change the observed local n, which most likely arises from the collapse of the polymer shell. For the subset of AuNR@pNIPAM$_{580}$ nanohybrids that exhibited increases in E_{res} at T_h (Table S3, Figure S8A), it is possible that the n of water decreased within the sensing volume of the AuNR and minimal polymer collapse occurred. It is also possible that pNIPAM readily collapsed when AuNR@pNIPAM$_{580}$ nanohybrids were colloidally suspended, but not when spincast on a substrate. However, Figure S8B and S8C show reversible collapse of the polymer and ~30% of AuNR@pNIPAM$_{580}$ nanohybrids exhibited decreases in energy greater than or equal to the ensemble ΔE_{res} (3.6 ± 0.4 meV) at T_h.

The complexity of the polymer collapse profile of the AuNR@pNIPAM$_{580}$ nanohybrids could result from a prominent two-step phase transition that was masked at the ensemble level such that the inner region VPT occurs at T_h and the outer region VPT only occurs at temperatures higher than T_h. Shan et al. reported that pNIPAM experienced two phase transitions on Au nanospheres and, as the polymer network chain length increased, the second phase transition broadened and shifted to lower temperatures.[35] The two phase transitions arose from (1) a densely packed inner region and (2) a hydrated coiled outer region.[35,36,79] The first region collapsed at the traditional VPTT, but the second region gradually collapsed over a broad range of temperatures.[79] Although Shan et al. did not introduce cross-linkers, we suspect that the two regions exist on a curved surface as presented by Reimhult and coworkers.[17] According to Reimhult et al., nanoparticle cores result in VPTs with multiple peaks distinguishable in DSC over larger temperature ranges than the LCST of linear pNIPAM chains.[17] Thus, we attribute the heterogeneity in ΔE_{res} and deviation from the ensemble behavior for AuNR@pNIPAM$_{580}$ nanohybrids to a two-step phase transition that exhibits a gradual collapse of the hydrated coiled outer region over a broad temperature range.[35,40]

Conclusions

Our study probes the influence of the internal heterogeneity of the polymer network of stimuli-responsive plasmonic nanohybrids on observed single-particle spectral changes and relates these observations to complex polymer phase transitions. In this study, we varied the AuNR E_{res} and the polymer shell thickness to investigate the influence of the core size and shell thickness on polymer phase transitions. We observed that the magnitude of ΔE_{res} was independent of the initial E_{res}, indicating a core size-independent polymer collapse. Contrary to ensemble observations, single-particle measurements revealed that the two polymer thicknesses investigated here did not have similar collapse profiles. For AuNR@pNIPAM$_{300}$ nanohybrids, we observed hysteresis in polymer collapse that likely resulted from interchain hydrogen bonds that persisted after the temperature decreased below the VPTT. For AuNR@pNIPAM$_{580}$ nanohybrids, we inferred a complex polymer collapse profile due to a two-step phase transition that ensemble UV-vis spectroscopy was unable to discern. These observed complex polymer phase transitions may be further compounded by the influence of the variable cross-linker density spanning the polymer shell on the local n observed by the core. It is evident, especially in the case of the thicker polymer shell, that commonly employed ensemble techniques, such as UV-vis spectroscopy, obscure the internal heterogeneity of the polymer network that influences the phase transitions of these nanohybrids. As a result, the observed polymer-induced E_{res} shifts were also more complex than current theoretical descriptions. Our single-particle approach revealed internal polymer network heterogeneity and is a promising step toward relating local differences in polymer chemistry to non-uniform VPT behavior. Using this single-particle approach, further work that varies the cross-linker concentrations could shed light on the influence of the cross-linker density on the collapse dynamics of polymer shells of similar thicknesses. Modifying the illumination geometry to achieve higher temperatures will further our understanding of the two-step phase transitions that we inferred for the AuNR@pNIPAM$_{580}$ nanohybrids. Further experimental work and updated theoretical descriptions are needed to quantify local differences in polymer chemistry at the nanoscale and relate these polymer properties to the mechanisms governing phase transitions, especially in the case of nanohybrids.

Acknowledgments

This work was primarily supported by the U.S. Department of Energy, Office of Science, Basic Energy Sciences, CPIMS Program, under Award # DE-339SC0016534. C.F. acknowledges support from the National Defense Science and Engineering Graduate Fellowship. C.D. and C.F.L. thank the National Science Foundation (grant no. CHE-1808382) and the Welch Foundation (grant no. C-1787). B.O. and S.L. thank the Welch Foundation (grant no. C-1664). This work was conducted in part using resources of the Shared Equipment Authority (SEA) at Rice University. The authors declare no competing financial interests.

Supporting Information

TEM and UV-vis spectroscopy characterization of AuNRs, temperature-controlled UV-vis spectroscopy of AuNRs, spectra of representative single particles prior to normalization, temperature-dependent refractive index changes of water, FDTD simulated scattering spectra for determining the sensing volume and substrate effect, comparison of the effect of the dielectric function of gold on the FDTD simulations, additional single-particle spectra, histograms of ΔE_{res} with and without heating, intensity changes at T_h.

References

(1) Cozzens, Y.; Steeves, D. M.; Soares, J. W.; Whitten, J. E. Light-Sensitive Gas Sensors Based on Thiol-Functionalized *N*-Isopropylacrylamide Polymer–Gold Nanoparticle Composite Films. *Macromolecules* **2019**, *52* (7), 2900–2910.

(2) Alarcón-Fernández, C.; Doña, M.; Tapia-Fernández, A.; Villaverde, G.; Lopez-Ramirez, M. R.; López-Romero, J. M.; Contreras-Caceres, R. Controlling Size and Morphology in Hybrid Core@Shell and Core@Shell@Satellite Nanostructures for Sensing by Surface-Enhanced Raman Scattering. *ACS Appl. Nano Mater.* **2020**, *3* (8), 8247–8256.

(3) Li, H.; Sentic, M.; Ravaine, V.; Sojic, N. Antagonistic Effects Leading to Turn-on Electrochemiluminescence in Thermoresponsive Hydrogel Films. *Phys. Chem. Chem. Phys.* **2016**, *18* (48), 32697–32702.

(4) Quilis, N. G.; Hageneder, S.; Fossati, S.; Auer, S. K.; Venugopalan, P.; Bozdogan, A.; Petri, C.; Moreno-Cencerrado, A.; Toca-Herrera, J. L.; Jonas, U.; et al. UV-Laser Interference Lithography for Local Functionalization of Plasmonic Nanostructures with Responsive Hydrogel. *J. Phys. Chem. C* **2020**, *124* (5), 3297–3305.

(5) Kawano, T.; Niidome, Y.; Mori, T.; Katayama, Y.; Niidome, T. PNIPAM Gel-Coated Gold Nanorods for Targeted Delivery Responding to a Near-Infrared Laser. *Bioconjugate Chem.* **2009**, *20* (2), 209–212.

(6) Zha, L.; Banik, B.; Alexis, F. Stimulus Responsive Nanogels for Drug Delivery. *Soft Matter* **2011**, *7* (13), 5908–5916.

(7) Walker, M.; Will, I.; Pratt, A.; Chechik, V.; Genever, P.; Ungar, D. Magnetically Triggered Release of Entrapped Bioactive Proteins from Thermally Responsive Polymer-Coated Iron Oxide Nanoparticles for Stem-Cell Proliferation. *ACS Appl. Nano Mater.* **2020**, *3* (6), 5008–5013.

(8) Matthews, B. M.; Maley, A. M.; Kartub, K. M.; Corn, R. M. Characterizing the Incorporation of DNA into Single NIPAm Hydrogel Nanoparticles with Surface Plasmon Resonance Imaging Measurements. *J. Phys. Chem. C* **2019**, *123* (10), 6090–6096.

(9) Li, S.; Lin, D.; Zhou, J.; Zha, L. Preparation of Silver Nanoparticles Loaded Photoresponsive Composite Microgels and Their Light-Controllable Catalytic Activity. *J. Phys. Chem. C* **2016**, *120* (9), 4902–4908.
(10) Gaitzsch, J.; Huang, X.; Voit, B. Engineering Functional Polymer Capsules toward Smart Nanoreactors. *Chem. Rev.* **2016**, *116* (3), 1053–1093.
(11) Eyimegwu, P. N.; Lartey, J. A.; Kim, J. H. Gold-Nanoparticle-Embedded Poly(N-Isopropylacrylamide) Microparticles for Selective Quasi-Homogeneous Catalytic Homocoupling Reactions. *ACS Appl. Nano Mater.* **2019**, *2* (9), 6057–6066.
(12) Maharjan, P.; Woonton, B. W.; Bennett, L. E.; Smithers, G. W.; DeSilva, K.; Hearn, M. T. W. Novel Chromatographic Separation — The Potential of Smart Polymers. *Innov. Food Sci. Emerg. Technol.* **2008**, *9* (2), 232–242.
(13) Schmidt, S.; Alberti, S.; Vana, P.; Soler-Illia, G. J. A. A.; Azzaroni, O. Thermosensitive Cation-Selective Mesochannels: PNIPAM-Capped Mesoporous Thin Films as Bioinspired Interfacial Architectures with Concerted Functions. *Chem. Eur. J.* **2017**, *23* (58), 14500–14506.
(14) Wu, D.; Honciuc, A. Design of Janus Nanoparticles with PH-Triggered Switchable Amphiphilicity for Interfacial Applications. *ACS Appl. Nano Mater.* **2018**, *1* (1), 471–482.
(15) Füllbrandt, M.; von Klitzing, R.; Schönhals, A. The Dielectric Signature of Poly(N-Isopropylacrylamide) Microgels at the Volume Phase Transition: Dependence on the Crosslinking Density. *Soft Matter* **2013**, *9* (17), 4464–4471.
(16) Contreras-Cáceres, R.; Sánchez-Iglesias, A.; Karg, M.; Pastoriza-Santos, I.; Pérez-Juste, J.; Pacifico, J.; Hellweg, T.; Fernández-Barbero, A.; Liz-Marzán, L. M. Encapsulation and Growth of Gold Nanoparticles in Thermoresponsive Microgels. *Adv. Mater.* **2008**, *20* (9), 1666–1670.
(17) Reimhult, E.; Schroffenegger, M.; Lassenberger, A. Design Principles for Thermoresponsive Core–Shell Nanoparticles: Controlling Thermal Transitions by Brush Morphology. *Langmuir* **2019**, *35* (22), 7092–7104.
(18) Karg, M.; Jaber, S.; Hellweg, T.; Mulvaney, P. Surface Plasmon Spectroscopy of Gold−Poly-*N*-Isopropylacrylamide Core−Shell Particles. *Langmuir* **2011**, *27* (2), 820–827.
(19) Lopez, C. G.; Scotti, A.; Brugnoni, M.; Richtering, W. The Swelling of Poly(Isopropylacrylamide) Near the θ Temperature: A Comparison between Linear and Cross-Linked Chains. *Macromol. Chem. Phys.* **2018**, *220*, 1800421.
(20) Kratz, K.; Hellweg, T.; Eimer, W. Effect of Connectivity and Charge Density on the Swelling and Local Structural and Dynamic Properties of Colloidal PNIPAM Microgels. *Ber. Bunsenges. Phys. Chem.* **1998**, *102* (11), 1603–1608.
(21) Li, L. Y.; He, W. D.; Li, W. T.; Zhang, K. R.; Pan, T. T.; Ding, Z. L.; Zhang, B. Y. Thermal and PH-Sensitive Gold Nanoparticles from H-Shaped Block Copolymers of (PNIPAM/PDMAEMA)-b-PEG-b-(PNIPAM/PDMAEMA). *J. Polym. Sci., Part A: Polym. Chem.* **2010**, *48* (22), 5018–5029.
(22) Koizumi, S.; Monkenbusch, M.; Richter, D.; Schwahn, D.; Farago, B.; Annaka, M. Frozen Concentration Fluctuations in a Poly(N-Isopropyl Acrylamide) Gel Studied by Neutron Spin Echo and Small-Angle Neutron Scattering. *Appl. Phys. A: Mater. Sci. Process.* **2002**, *74* (0), s399–s401.
(23) Boon, N.; Schurtenberger, P. Swelling of Micro-Hydrogels with a Crosslinker Gradient. *Phys. Chem. Chem. Phys.* **2017**, *19* (35), 23740–23746.
(24) Wu, C.; Zhou, S. Volume Phase Transition of Swollen Gels: Discontinuous or Continuous? *Macromolecules* **1997**, *30* (3), 574–576.
(25) Stieger, M.; Richtering, W.; Pedersen, J. S.; Lindner, P. Small-Angle Neutron Scattering Study of Structural Changes in Temperature Sensitive Microgel Colloids. *J. Chem. Phys.* **2004**, *120* (13), 6197–6206.
(26) Dulle, M.; Jaber, S.; Rosenfeldt, S.; Radulescu, A.; Förster, S.; Mulvaney, P.; Karg, M. Plasmonic Gold–Poly(N-Isopropylacrylamide) Core–Shell Colloids with Homogeneous Density Profiles: A Small Angle Scattering Study. *Phys. Chem. Chem. Phys.* **2014**, *17* (2), 1354–1367.

(27) Fernández-López, C.; Polavarapu, L.; Solís, D. M.; Taboada, J. M.; Obelleiro, F.; Contreras-Cáceres, R.; Pastoriza-Santos, I.; Pérez-Juste, J. Gold Nanorod–PNIPAM Hybrids with Reversible Plasmon Coupling: Synthesis, Modeling, and SERS Properties. *ACS Appl. Mater. Interfaces* **2015**, *7* (23), 12530–12538.
(28) Zhao, J.; Su, H.; Vansuch, G. E.; Liu, Z.; Salaita, K.; Dyer, R. B. Localized Nanoscale Heating Leads to Ultrafast Hydrogel Volume-Phase Transition. *ACS Nano* **2019**, *13* (1), 515–525.
(29) Nguyen, H. H.; Payré, B.; Fitremann, J.; Lauth-de Viguerie, N.; Marty, J. D. Thermoresponsive Properties of PNIPAM-Based Hydrogels: Effect of Molecular Architecture and Embedded Gold Nanoparticles. *Langmuir* **2015**, *31* (16), 4761–4768.
(30) Murphy, S.; Jaber, S.; Ritchie, C.; Karg, M.; Mulvaney, P. Laser Flash Photolysis of Au-PNIPAM Core–Shell Nanoparticles: Dynamics of the Shell Response. *Langmuir* **2016**, *32* (47), 12497–12503.
(31) Wu, C.; Wang, X. Globule-to-Coil Transition of a Single Homopolymer Chain in Solution. *Phys. Rev. Lett.* **1998**, *80* (18), 4092–4094.
(32) Cheng, H.; Shen, L.; Wu, C. LLS and FTIR Studies on the Hysteresis in Association and Dissociation of Poly(N-Isopropylacrylamide) Chains in Water. *Macromolecules* **2006**, *39* (6), 2325–2329.
(33) Yeshchenko, O. A.; Naumenko, A. P.; Kutsevol, N. V.; Maskova, D. O.; Harahuts, I. I.; Chumachenko, V. A.; Marinin, A. I. Anomalous Inverse Hysteresis of Phase Transition in Thermosensitive Dextran- *Graft* -PNIPAM Copolymer/Au Nanoparticles Hybrid Nanosystem. *J. Phys. Chem. C* **2018**, *122* (14), 8003–8010.
(34) Luo, S.; Xu, J.; Zhu, Z.; Wu, C.; Liu, S. Phase Transition Behavior of Unimolecular Micelles with Thermoresponsive Poly(N-Isopropylacrylamide) Coronas. *J. Phys. Chem. B* **2006**, *110* (18), 9132–9139.
(35) Shan, J.; Chen, J.; Nuopponen, M.; Tenhu, H. Two Phase Transitions of Poly(N-Isopropylacrylamide) Brushes Bound to Gold Nanoparticles. *Langmuir* **2004**, *20* (11), 4671–4676.
(36) Zhang, Y.; Luo, S.; Liu, S. Fabrication of Hybrid Nanoparticles with Thermoresponsive Coronas via a Self-Assembling Approach. *Macromolecules* **2005**, *38* (23), 9813–9820.
(37) Fernández-Barbero, A.; Fernández-Nieves, A.; Grillo, I.; López-Cabarcos, E. Structural Modifications in the Swelling of Inhomogeneous Microgels by Light and Neutron Scattering. *Phys. Rev. E* **2002**, *66* (5), 051803.
(38) Karg, M.; Hellweg, T. New “Smart” Poly(NIPAM) Microgels and Nanoparticle Microgel Hybrids: Properties and Advances in Characterisation. *Curr. Opin. Colloid Interface Sci.* **2009**, *14* (6), 438–450.
(39) Harrer, J.; Rey, M.; Ciarella, S.; Löwen, H.; Janssen, L. M. C.; Vogel, N. Stimuli-Responsive Behavior of PNiPAm Microgels under Interfacial Confinement. *Langmuir* **2019**, *35* (32), 10512–10521.
(40) Kratz, K.; Hellweg, T.; Eimer, W. Structural Changes in PNIPAM Microgel Particles as Seen by SANS, DLS, and EM Techniques. *Polymer* **2001**, *42* (15), 6631–6639.
(41) Marchand, D. J.; Hsiao, E.; Kim, S. H. Non-Contact AFM Imaging in Water Using Electrically Driven Cantilever Vibration. *Langmuir* **2013**, *29* (22), 6762–6769.
(42) Wiedemair, J.; Serpe, M. J.; Kim, J.; Masson, J. F.; Lyon, L. A.; Mizaikoff, B.; Kranz, C. In-Situ AFM Studies of the Phase-Transition Behavior of Single Thermoresponsive Hydrogel Particles. *Langmuir* **2007**, *23* (1), 130–137.
(43) Denoual, M.; Menon, V.; Sato, T.; de Sagazan, O.; Coleman, A. W.; Fujita, H. Liquid Cell with Temperature Control for *in Situ* TEM Chemical Studies. *Meas. Sci. Technol.* **2019**, *30* (1), 017001.
(44) Kirchner, S. R.; Smith, K. W.; Hoener, B. S.; Collins, S. S. E.; Wang, W.; Cai, Y. Y.; Kinnear, C.; Zhang, H.; Chang, W. S.; Mulvaney, P.; et al. Snapshot Hyperspectral Imaging (SHI) for Revealing Irreversible and Heterogeneous Plasmonic Processes. *J. Phys. Chem. C* **2018**, *122* (12), 6865–6875.

(45) Flatebo, C.; Collins, S. S. E.; Hoener, B. S.; Cai, Y. Y.; Link, S.; Landes, C. F. Electrodissolution Inhibition of Gold Nanorods with Oxoanions. *J. Phys. Chem. C* **2019**, *123* (22), 13983–13992.
(46) Byers, C. P.; Hoener, B. S.; Chang, W. S.; Yorulmaz, M.; Link, S.; Landes, C. F. Single-Particle Spectroscopy Reveals Heterogeneity in Electrochemical Tuning of the Localized Surface Plasmon. *J. Phys. Chem. B* **2014**, *118* (49), 14047–14055.
(47) Hoppe Alvarez, L.; Eisold, S.; Gumerov, R. A.; Strauch, M.; Rudov, A. A.; Lenssen, P.; Merhof, D.; Potemkin, I. I.; Simon, U.; Wöll, D. Deformation of Microgels at Solid–Liquid Interfaces Visualized in Three-Dimension. *Nano Lett.* **2019**, *19* (12), 8862–8867.
(48) Dutta, C.; Bishop, L. D. C.; Zepeda O, J.; Chatterjee, S.; Flatebo, C.; Landes, C. F. Imaging Switchable Protein Interactions with an Active Porous Polymer Support. *J. Phys. Chem. B* **2020**, *124* (22), 4412–4420.
(49) Anger, P.; Bharadwaj, P.; Novotny, L. Enhancement and Quenching of Single-Molecule Fluorescence. *Phys. Rev. Lett.* **2006**, *96* (11), 113002.
(50) Rauh, A.; Honold, T.; Karg, M. Seeded Precipitation Polymerization for the Synthesis of Gold-Hydrogel Core-Shell Particles: The Role of Surface Functionalization and Seed Concentration. *Colloid Polym. Sci.* **2016**, *294* (1), 37–47.
(51) Rusu, M.; Wohlrab, S.; Kuckling, D.; Möhwald, H.; Schönhoff, M. Coil-to-Globule Transition of PNIPAM Graft Copolymers with Charged Side Chains: A 1H and 2H NMR and Spin Relaxation Study. *Macromolecules* **2006**, *39* (21), 7358–7363.
(52) Contreras-Cáceres, R.; Pacifico, J.; Pastoriza-Santos, I.; Pérez-Juste, J.; Fernández-Barbero, A.; Liz-Marzán, L. M. Au@pNIPAM Thermosensitive Nanostructures: Control over Shell Cross-Linking, Overall Dimensions, and Core Growth. *Adv. Funct. Mater.* **2009**, *19* (19), 3070–3076.
(53) Li, M.; Cushing, S. K.; Wu, N. Plasmon-Enhanced Optical Sensors: A Review. *Analyst* **2015**, *140* (2), 386–406.
(54) Mock, J. J.; Smith, D. R.; Schultz, S. Local Refractive Index Dependence of Plasmon Resonance Spectra from Individual Nanoparticles. *Nano Lett.* **2003**, *3* (4), 485–491.
(55) Tagliazucchi, M.; Blaber, M. G.; Schatz, G. C.; Weiss, E. A.; Szleifer, I. Optical Properties of Responsive Hybrid Au@Polymer Nanoparticles. *ACS Nano* **2012**, *6* (9), 8397–8406.
(56) Link, S.; El-Sayed, M. A. Spectral Properties and Relaxation Dynamics of Surface Plasmon Electronic Oscillations in Gold and Silver Nanodots and Nanorods. *J. Phys. Chem. B* **1999**, *103* (40), 8410–8426.
(57) Ye, X.; Zheng, C.; Chen, J.; Gao, Y.; Murray, C. B. Using Binary Surfactant Mixtures to Simultaneously Improve Dimensional Tunability and Monodispersity in the Seeded-Growth of Gold Nanorods. *Nano Lett.* **2013**, *13* (2), 765–771.
(58) Contreras-Cáceres, R.; Pastoriza-Santos, I.; Alvarez-Puebla, R. A.; Pérez-Juste, J.; Fernández-Barbero, A.; Liz-Marzán, L. M. Growing Au/Ag Nanoparticles within Microgel Colloids for Improved Surface-Enhanced Raman Scattering Detection. *Chem. Eur. J.* **2010**, *16* (31), 9462–9467.
(59) Jaber, S. Synthesis and Self-Assembly of Core-Shell Gold Nanorod-PNIPAM Nanoparticles. PhD Thesis, University of Melbourne, Melbourne, Australia, 2016.
(60) Gudjonson, H.; Kats, M. A.; Liu, K.; Nie, Z.; Kumacheva, E.; Capasso, F. Accounting for Inhomogeneous Broadening in Nano-Optics by Electromagnetic Modeling Based on Monte Carlo Methods. *Proc. Natl. Acad. Sci. USA* **2014**, *111* (6), E639–E644.
(61) Jain, P. K.; Huang, W.; El-Sayed, M. A. On the Universal Scaling Behavior of the Distance Decay of Plasmon Coupling in Metal Nanoparticle Pairs: A Plasmon Ruler Equation. *Nano Lett.* **2007**, *7* (7), 2080–2088.
(62) Braun, J. L.; Hopkins, P. E. Upper Limit to the Thermal Penetration Depth during Modulated Heating of Multilayer Thin Films with Pulsed and Continuous Wave Lasers: A Numerical Study. *J. Appl. Phys.* **2017**, *121* (17), 175107.

(63) Vizcay-Barrena, G.; Webb, S. E. D.; Martin-Fernandez, M. L.; Wilson, Z. A. Subcellular and Single-Molecule Imaging of Plant Fluorescent Proteins Using Total Internal Reflection Fluorescence Microscopy (TIRFM). *J. Exp. Biol.* **2011**, *62* (15), 5419–5428.
(64) Moerland, R. J.; Hoogenboom, J. P. Subnanometer-Accuracy Optical Distance Ruler Based on Fluorescence Quenching by Transparent Conductors. *Optica* **2016**, *3* (2), 112–117.
(65) Li, C. H.; Lin, H. K. Effect of Wavelength on the Laser Patterning of a Cholesteric Liquid Crystal Display Electrode. *Thin Solid Films* **2013**, *529*, 222–225.
(66) Sönnichsen, C.; Franzl, T.; Wilk, T.; von Plessen, G.; Feldmann, J.; Wilson, O.; Mulvaney, P. Drastic Reduction of Plasmon Damping in Gold Nanorods. *Phys. Rev. Lett.* **2002**, *88* (7), 077402.
(67) Perner, M.; Klar, T.; Grosse, S.; Lemmer, U.; von Plessen, G.; Spirkl, W.; Feldmann, J. Homogeneous Line Widths of Surface Plasmons in Gold Nanoparticles Measured by Femtosecond Pump-and-Probe and near-Field Optical Spectroscopy. *J. Lumin.* **1998**, *76–77*, 181–184.
(68) van der Walt, S.; Schönberger, J. L.; Nunez-Iglesias, J.; Boulogne, F.; Warner, J. D.; Yager, N.; Gouillart, E.; Yu, T. Scikit-Image: Image Processing in Python. *PeerJ* **2014**, *2*, e453.
(69) Johnson, P. B.; Christy, R. W. Optical Constants of the Noble Metals. *Phys. Rev. B* **1972**, *6* (12), 4370–4379.
(70) Olmon, R. L.; Slovick, B.; Johnson, T. W.; Shelton, D.; Oh, S.-H.; Boreman, G. D.; Raschke, M. B. Optical Dielectric Function of Gold. *Phys. Rev. B* **2012**, *86* (23), 235147.
(71) Thormählen, I.; Straub, J.; Grigull, U. Refractive Index of Water and Its Dependence on Wavelength, Temperature, and Density. *J. Phys. Chem. Ref. Data* **1985**, *14* (4), 933–945.
(72) Reufer, M.; Dıaz-Leyva, P.; Lynch, I.; Scheffold, F. Temperature-Sensitive Poly(N-Isopropyl-Acrylamide) Microgel Particles: A Light Scattering Study. *Eur. Phys. J. E* **2009**, *28* (2), 165–171.
(73) Martinsson, E.; Aili, D. Refractometric Sensing Using Plasmonic Nanoparticles. In *Encyclopedia of Nanotechnology*; Bhushan, B., Ed.; Springer Netherlands: Dordrecht, 2016; pp 3432–3440.
(74) Schweizerhof, S.; Demco, D. E.; Mourran, A.; Fechete, R.; Möller, M. Diffusion of Gold Nanorods Functionalized with Thermoresponsive Polymer Brushes. *Langmuir* **2018**, *34* (27), 8031–8041.
(75) Feller, D.; Otten, M.; Hildebrandt, M.; Krüsmann, M.; Bryant, G.; Karg, M. Translational and Rotational Diffusion Coefficients of Gold Nanorods Functionalized with a High Molecular Weight, Thermoresponsive Ligand: A Depolarized Dynamic Light Scattering Study. *Soft Matter* **2021**, *17* (15), 4019–4026.
(76) Ingham, J. D.; Lawson, D. D. Refractive Index–Molecular Weight Relationships for Poly(Ethylene Oxide). *J. Polym. Sci., Part A: Gen. Pap.* **1965**, *3* (7), 2707–2710.
(77) Heinz, P.; Brétagnol, F.; Mannelli, I.; Gillil, D.; Rauscher, H.; Rossi, F. Phase Transition of PNIPAM Grafted on Plasma-Activated PEO Monitored *in-Situ* by Quartz Crystal Microbalance. *J. Phys.: Conf. Ser.* **2008**, *100* (1), 012033.
(78) Yanase, K.; Buchner, R.; Sato, T. Microscopic Insights into the Phase Transition of Poly(N-Isopropylacrylamide) in Aqueous Media: Effects of Molecular Weight and Polymer Concentration. *J. Mol. Liq.* **2020**, *302*, 112025.
(79) Balamurugan, S.; Mendez, S.; Balamurugan, S. S.; O'Brien, M. J.; López, G. P. Thermal Response of Poly(*N*-Isopropylacrylamide) Brushes Probed by Surface Plasmon Resonance. *Langmuir* **2003**, *19* (7), 2545–2549.
(80) Plunkett, K. N.; Zhu, X.; Moore, J. S.; Leckband, D. E. PNIPAM Chain Collapse Depends on the Molecular Weight and Grafting Density. *Langmuir* **2006**, *22* (9), 4259–4266.

TOC Graphic

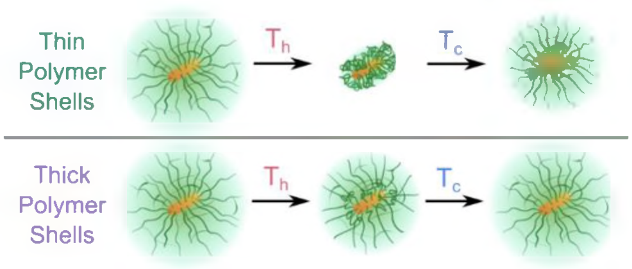
Thin
Polymer
Shells
Th
Tc
Thick
Polymer
Shells
Th
Tc